Powder Technology 338 (2018) 253–262

Contents lists available at ScienceDirect

Powder Technology

journal homepage: www.elsevier.com/locate/powtec

Jamming during particle spreading in additive manufacturing

Wenguang Nan [a,b], Mehrdad Pasha [a], Tina Bonakdar [a], Alejandro Lopez [a], Umair Zafar [a], Sadegh Nadimi [a], Mojtaba Ghadiri [a,*]

[a] Faculty of Engineering, University of Leeds, Leeds LS2 9JT, UK
[b] School of Mechanical and Power Engineering, Nanjing Tech University, Nanjing 211816, China

ARTICLE INFO

Article history:
Received 7 May 2018
Received in revised form 3 July 2018
Accepted 6 July 2018
Available online xxxx

Keywords:
Additive manufacturing
Particle spreading
Sintering
Jamming
Discrete element method
Non-spherical particle

ABSTRACT

Additive manufacturing (AM) is going through an exponential growth, due to its enormous potential for rapid manufacturing of complex shapes. One of the manufacturing methods is based on powder processing, but its major bottleneck is associated with powder spreading, as mechanical arching adversely affects both product quality and speed of production. Here we analyse transient jamming of gas-atomised metal powders during spreading. These particles are highly frictional, as they have asperities and multiple spheres and are prone to jamming in narrow gaps. Therefore their detailed characterisations of mechanical properties are critical to be able to reliably predict the jamming frequency as influenced by powder properties and process conditions. Special methods have been used to determine the physical and mechanical properties of gas-atomised stainless steel powders. These properties are then used in numerical simulations of powder spreading by the Discrete Element Method. Particle shape is reconstructed for the simulations as a function of particle size. The characteristic size D_{90} by number (i.e. the particle size, based on the projected-area diameter, for which 90% of particles by number are smaller than this value) is used as the particle dimension accountable for jamming. Jamming is manifested by empty patches over the work surface. Its frequency and period have been characterised as a function of the spreader gap height, expressed as multiple of D_{90}. The probability of formation of empty patches and their mean length, the latter indicating jamming duration, increase sharply with the decrease of the gap height. The collapse of the mechanical arches leads to particle bursts after the blade. The frequency of jamming for a given survival time decreases exponentially as the survival time increases.

1. Introduction

Additive manufacturing (AM) has been widely explored in a wide range of applications, such as aerospace, biology, medicine and architecture [1–5]. As a novel production technology, additive manufacturing is able to create a three-dimensional object directly from the Computer-Aided Design (3D CAD) system without the need for expensive tooling and much time [6–8]. It is going through an exponential growth, due to its enormous potential for rapid manufacturing of complex or customized shapes. There are several manufacturing methods, ranging from 3D printing from a liquid-based feed [9,10] to powder-based process [11,12], in which typically 10–50 μm particles are spread over a particle bed (already partially sintered/melted) by a roller or blade, resulting in a particle layer with thickness of a few particle diameters. Then a laser or electron beam is shone onto the particle layer to melt the specified area. Once a cross section is scanned, the particle bed is lowered and the process is repeated until the completion of the production. Powder-based methods do not require the formulation of the liquid feed and are more flexible, thus attracting increasing attention. However, powders suitable for such applications should have small particle size for rapid sintering and melting, and therefore they exhibit a host of processing problems that are well-known to process engineers, such as arching [13], inconsistent flow and sensitivity to operation speed. This situation is exacerbated in AM as the powder layer should be sufficiently thin (i.e. a few particle diameters) for energy beam application. As the powder is spread by a blade or roller with a small gap height, mechanical arching and transient jamming are more prevalent [14]. The situation could further deteriorate at high operation speeds, producing patchy coverage, leading to defects in the product.

Lack of sufficient understanding of the multi-physics process, such as cohesive and frictional powder flow in the spreading process [5,15] and heat transfer [16,17] in the sintering process, hinder further development of this technology and introduction of new materials [18,19]. The powder spreading process has an important effect on the characteristics and quality of the final product. For example, empty patches might form in the particle layer leading to weak bonding between particles in the sintering process [20,21]. These limitations result in expensive trial-and-error and uncertainty in the quality of final products. Therefore problems associated with powder spreading are major manufacturing

* Corresponding author.
E-mail address: M.Ghadiri@leeds.ac.uk (M. Ghadiri).

https://doi.org/10.1016/j.powtec.2018.07.030

bottlenecks, adversely affecting product quality and throughput. Once a solid specimen is made by this method, it is not easy to diagnose the presence of flaws. So understanding of factors which give rise to patchy powder spreading is highly desirable.

Recently, the Discrete Element Method (DEM) has been used to explore the fundamentals of particle layering in the additive manufacturing. Haeri et al. [22] investigated the effects of aspect ratio of rod-like particles and operation conditions on the bed quality. They found large particle aspect ratio and high spreader translational velocity could lead to low bed quality. Parteli and Pöschel [23] used a roller as the spreading system and found that particles with a broad size distribution could lead to large values of surface roughness as the smaller particles were more prone to form large agglomerates, thus increasing the bed porosity. Xiang et al. [24] simulated the forming process of a particle bed, in which the process was simplified as random packing, layering, and compression, and showed that the packing density and average coordination number increased with the layer thickness. Haeri [25] evaluated the performance of several blade geometries, spreading particles with shapes represented by overlapping spheres, and concluded that a super-elliptic edge profile for the spreader produces a bed with volume fraction and surface roughness that is comparable to that made by a roller. Based on the DEM simulation of spreading of spherical particles, Chen et al. [26] found that decreasing particle friction coefficient could lead to a denser and more uniform particle bed, whilst increasing cohesion between particles reduced the quality of particle layer. Large gaps between the spreader and bed surface in the actual production could sacrifice the dimensional accuracy of manufactured parts to some degree; so it is necessary to explore the powder spreading with small gaps to improve the product quality. Meanwhile, the particle properties and simulation conditions in these works did not fully represent those of real particles in AM, as the particle shape with high fidelity or mechanical properties of particles (including Young's Modulus, interfacial surface energy, coefficient of sliding friction and so on) were not always used in the simulations. Moreover they mainly focussed on the volume fraction and roughness as well as micro-structure of the final particle layer, and did not address particle dynamics in the region near the blade, which gives rise to jamming.

We report on our analysis of the effect of gap height on particle dynamics and transient jamming based on numerical simulations using Discrete Element Method (DEM). The particle bed comprises gas-atomised stainless steel particles, with their physical and mechanical properties extensively characterised as described below. A heap of particles is subjected to a translational motion by a vertical blade with a gap allowing a thin particle layer to be spread. The particle dynamics around the blade, the empty patches and their formation mechanism are analysed. This provides a step towards understanding the details of spreading process of realistic particles.

2. Particle characterisation

Gas-atomised 316 L stainless steel particles, provided by Sandvik Osprey Ltd., Neath, UK, are used in this work for characterisation of their physical and mechanical properties, as needed for numerical simulations. Prior to the characterisation work, the particle sample is subdivided by a spinning riffler to get representative small samples for analysis.

2.1. Size and shape distributions

To characterise the size and shape distributions of the particles, a representative sample as obtained above, is dispersed using the dispersion unit of Morphologi G3 (Malvern Panalytical Ltd., Malvern, UK) at 3 Barg with 20 ms of pressure pulse injection time, and a number of images of dispersed particles are taken by SEM and analysed by Avizo Fire (FEI Visualization Sciences Group, Germany), as shown in Fig. 1. The sample quantity, dispersion pressure and injection time are set to ensure uniform dispersion and to mitigate particles settling over each other. The image analysis shows that the particles have a size distribution in the range 15–55 μm, for which the number based D_{10}, D_{50} and D_{90} are 20 μm, 32 μm and 45 μm, respectively. Based on the equivalent-circle diameter of the projected area at rest, 2500 particles are classified into four main size classes, as shown in Fig. 2. In the following sections, D_{90} is denoted by D for simplicity.

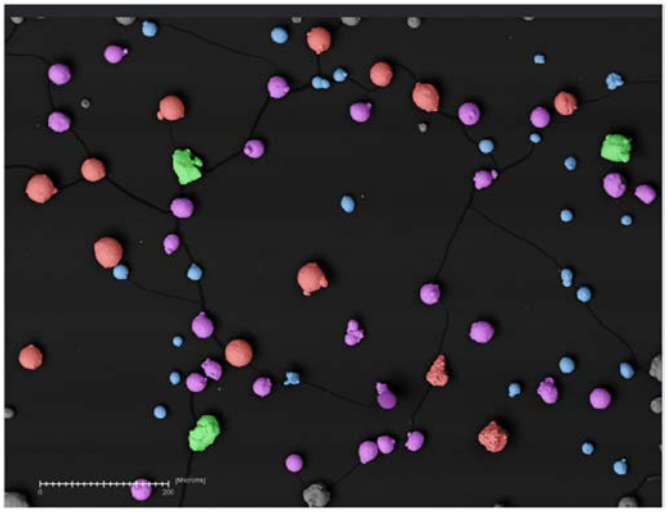

Fig. 1. SEM images of gas atomised steel powder. The particles are coloured based on their size: blue (15–25 μm), purple (25–35 μm), red (35–45 μm), and green (45–55 μm). (For interpretation of the references to colour in this figure legend, the reader is referred to the web version of this article.)

Particle shape has a significant impact on particle dynamics in the spreading process [22]. Therefore, accurate representation of particle shape is indispensable for reliable simulation of particle flow in additive manufacturing. Microscopic observations show that particle shape varies with particle size, where smaller particles tend to be more spherical as compared to larger ones (i.e. 15–25 μm and 45–55 μm), as shown in Fig. 1. So for each size class, 5–10 particles are randomly selected for simulating their shapes. Here, the complex particle shape is modelled by the overlapping multi-sphere method as described by Favier et al. [27], and shown in Fig. 3. Each particle is approximated by a number of overlapping spheres of different sizes, following the multi-sphere approximation approach of Pasha et al. [28].

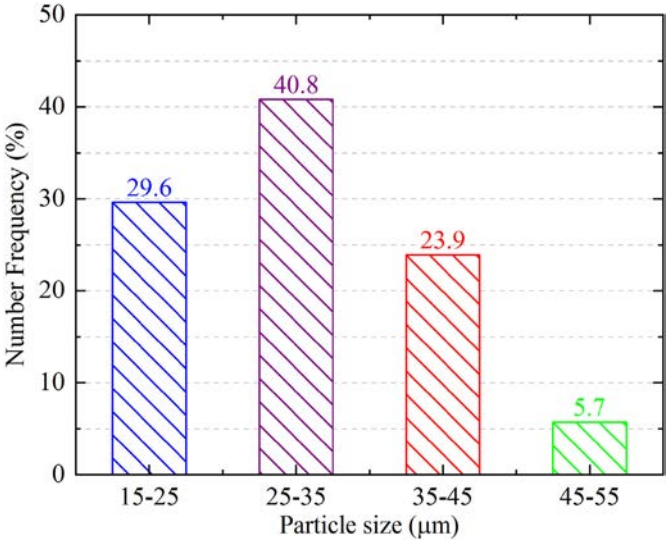

Fig. 2. Particle size distribution (equivalent-circle diameter) of gas atomised steel powder with four size classes.

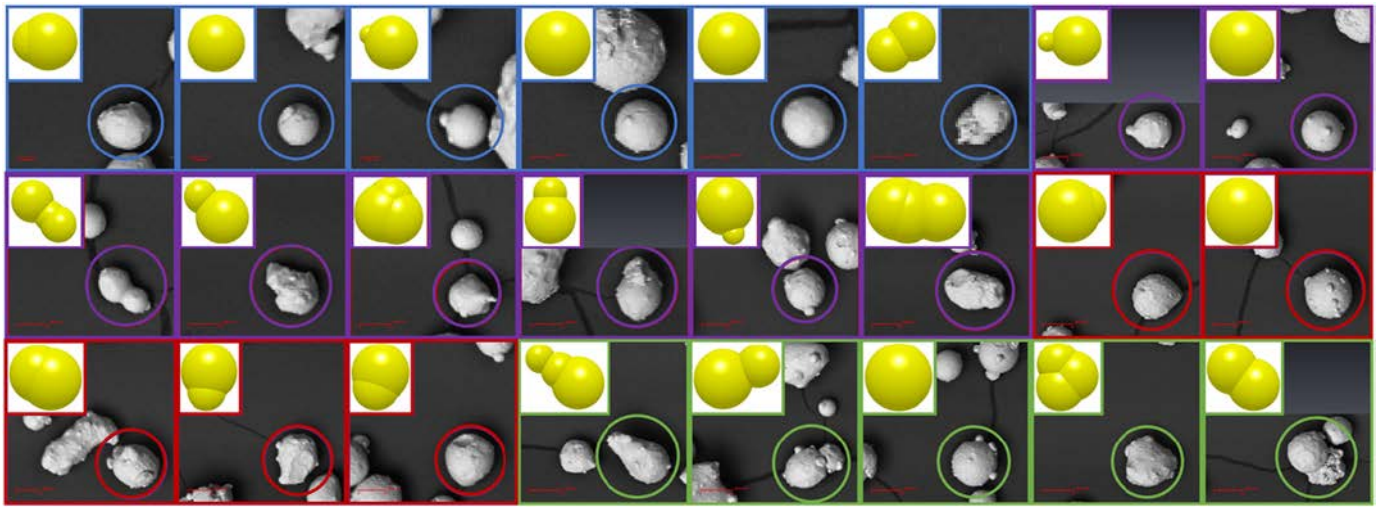

Fig. 3. Particle shapes used in DEM simulations; each size and shape class are represented by a colour circle, as shape varies with size; six blue circles (15–25 μm), eight purple circles (25–35 μm), five red circles (35–45 μm), and five green circles (45–55 μm). (For interpretation of the references to colour in this figure legend, the reader is referred to the web version of this article.)

2.2. Mechanical properties: hardness and Young's modulus

The hardness and Young's modulus of the particles are measured by nano-indentation technique using a NanoTest® Platform 3 machine (Micro Materials Ltd., Wrexham, UK) following the approach described by Ghadiri [29]. Indentation on surfaces of small particles is difficult due to surface curvature. Therefore the particles are imbedded in resin and polished to present a flat surface for indentation. The indenter is driven into the surface of an individual particle at a fixed loading rate of 0.5mN/s until a pre-defined maximum depth is obtained. The sample stage is then repositioned for indentation onto another particle. A sensitivity analysis is done using different indentation loads to investigate an acceptable range for indentation depth, based on which a maximum depth of 300 nm is used. Many indentations are made and the indents are then observed under SEM to validate them. Those indents which cannot be found or the indent shape is unrealistically skewed are discarded. The SEM images of some successful indents are shown in Fig. 4. Based on nine successful measurements on different particles, the average values of hardness and Young's modulus are 2.90 and 211GPa, and their standard deviations are 0.18 and 30 GPa, respectively, assuming a Poisson's ratio of 0.3.

2.3. Interfacial surface energy

Metals have large surface energy, therefore for fine metal particles the attractive forces due to van der Waals could be sufficiently large to influence the powder flow. The interfacial adhesive surface energy is measured by the newly-developed Drop Test Method [30], by which the particles are subjected to a transient tensile force, produced by impact and the interfacial surface energy is inferred from Johnson, Kendall and Roberts analysis [31]. A sample of test particles are dispersed on a polished steel plate of 6 mm diameter and 2 mm thickness, which is stuck to an aluminium stub. The dispersion is carried out using the same procedure as of the particle size and shape analyses described above using a bulk powder volume of 7 mm^3, giving roughly around 1500 particles on the steel plate. Following this step images of particles on the steel substrate are recorded by Morphologi G3. The particles are then subjected to impact test at different velocities, ranging from 0.5 to 2.0 m/s, measured by a Photron FASTCAM SA5 high speed video camera at 75,000 frames per second. Three repeats are carried out for each test. A typical successful impact test for the particles used in this work has an average impact velocity and contact time of 0.98 m/s and 520 μs, respectively. In order to calculate the interfacial surface energy, the critical particle diameter, for which the force balance is made between adhesion and detachment momentum, is measured as 36 μm, based on the scanned images of around 300–400 particles after the tests for the three repeats. For illustration, SEM images of adhered particles before and after one of the impact tests are shown in Fig. 5 as an example. The particles marked blue are those which detach, and those marked red are the largest ones which have remained attached, from which the critical particle size for detachment is estimated. Based on the balance between the force of adhesion by JKR model [31] and force of detachment by Newton's second law of motion, a unique interfacial surface energy is calculated as 9 mJ/m^2 for stainless steel particles in contact with the steel plate.

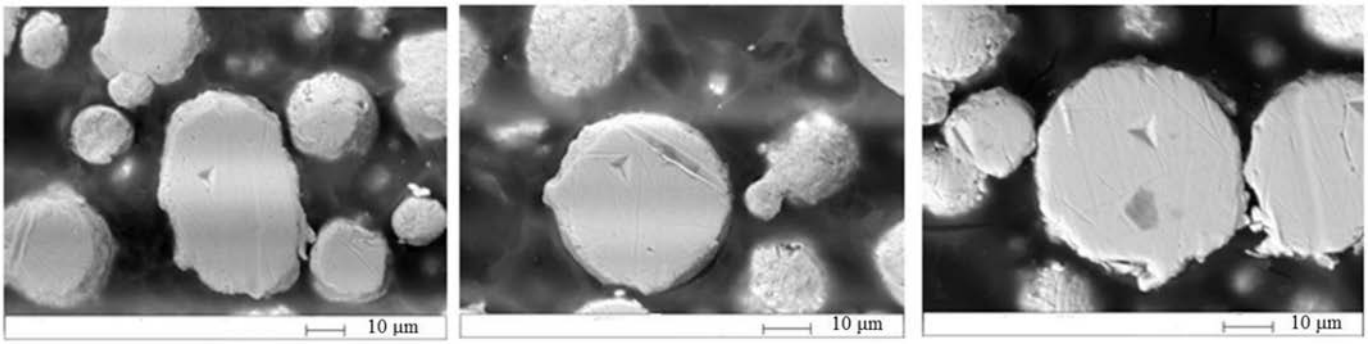

Fig. 4. Typical SEM images of successful indents.

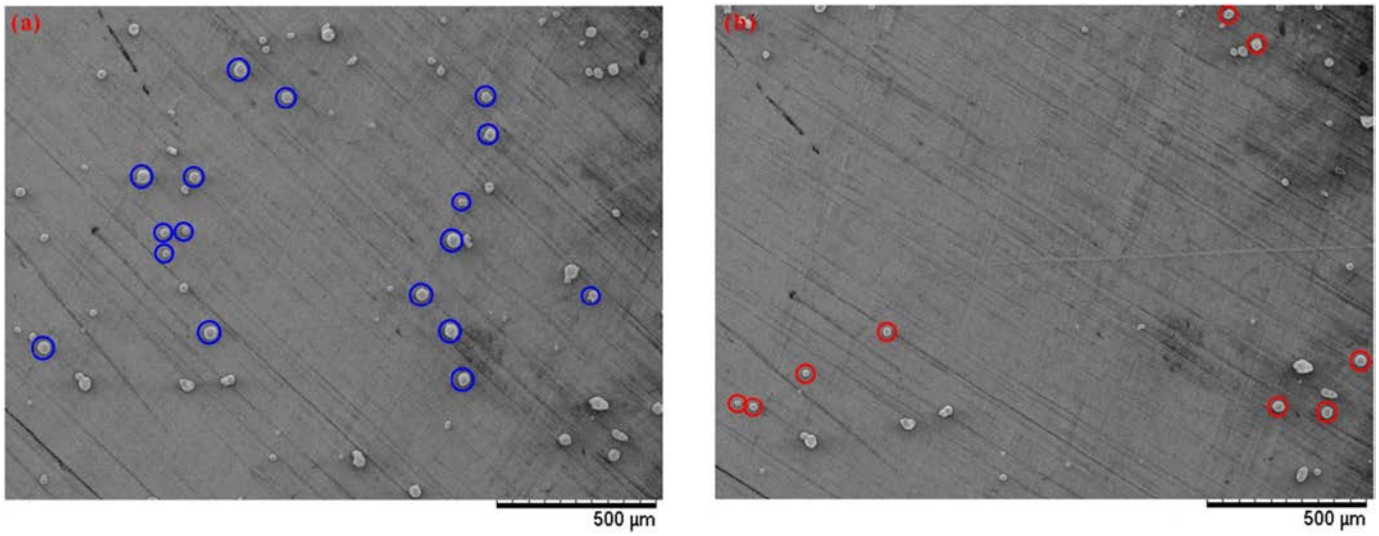

Fig. 5. Example of particle detachment: SEM images (a) before the impact; (b) after the impact.

2.4. Coefficient of restitution

This is obtained by image analysis of impacts of particles against a stainless steel substrate recorded by Photron FASTCAM SA5at 6000 frames per second. To mitigate the effect of weak air current in the laboratory on the particle trajectory, an enclosure is set up around the experimental rig. The particles are fed by using a modified vibratory feeder in which the outlet size is constricted to allow a small number of particles passing through at a time. The individual pre and post-rebound maximum velocities are analysed by ImageJ software, using the particle tracking algorithm developed by Sbalzarini and Koumoutsakos [32]. The restitution coefficient is measured for 68 particles and its average value is 0.64 with a standard deviation of 0.084. Only normal rebounds are considered and inclined or rotational rebounds discarded.

2.5. Coefficient of sliding friction

A new in-house method has been developed for measuring particle sliding friction for use in DEM simulations. The steel powder is deposited onto a flat glass slide using a superglue as shown in Fig. 6. Special care is taken to ensure the particles top surfaces are not covered by the superglue. The prepared slide is then placed face down against an additively-manufactured steel plate with the same texture as the surface over which the powder bed is spread, shown in Fig. 6(c). The AM steel plate is then tilted up to an angle at which the slide starts sliding down as shown in Fig. 6(d). At this point, the corresponding angle is recorded. This process is repeated several times to increase the reliability of the measurements. This angle is dominated by roughness of AM steel plate and steel powder. The surfaces in DEM simulations are smooth,

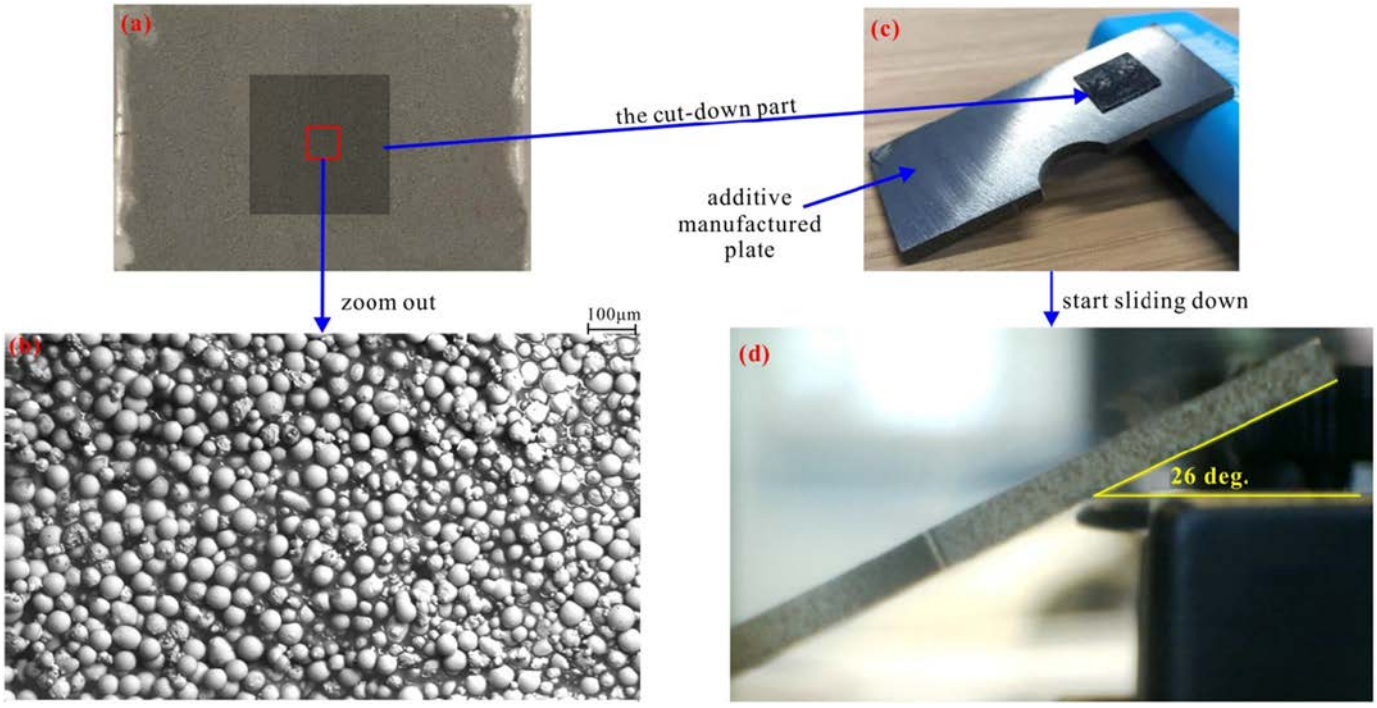

Fig. 6. Measurement of friction coefficient: (a) deposition of steel powder onto a glass slide; (b) SEM image of the deposited layer; (c, d) process of setting and measuring the angle of sliding for steel powder plate and AM steel plate.

therefore to account for the effect of roughness, the friction coefficient is calibrated. To do so, a series of DEM simulations are carried out to match the sliding angle of the plate by tuning the particle friction coefficient. To maximise the accuracy of this calibration process, the measured properties discussed in the previous sections are used here (i.e. particle shape, coefficient of restitution, Young's modulus, interfacial surface energy, etc.). Based on this method, the calibrated value of sliding friction coefficient for gas-atomised steel powder used in this study is 0.5.

3. Method

3.1. Discrete element method

To describe the dynamics of particle flow in the spreading process, the particles are modelled as discrete entities and their motions are tracked individually by solving Newton's laws of motion [33,34], for which the EDEM™ software package provided by DEM Solutions, Edinburgh, UK, is used. For completeness, we only describe the key features of the simulation method below and further information is given by Nan et al. [35]. In this approach, the movement of an individual particle is described by the translational and rotational motion, given by:

$$m_i \frac{d\boldsymbol{v}_i}{dt} = \sum \boldsymbol{F}_{c,i} + m_i \boldsymbol{g} \tag{1}$$

$$\frac{d(\boldsymbol{I}_i \cdot \boldsymbol{\omega}_i)}{dt} = \boldsymbol{R}_i \cdot \sum \boldsymbol{M}_{c,i} \tag{2}$$

where m_i, $\boldsymbol{I}_i$, $\boldsymbol{v}_i$ and $\boldsymbol{\omega}_i$ are the mass, moment of inertia, translational velocity and angular velocity, respectively; $\boldsymbol{F}_{c,i}$ is the contact force, originating from its interaction with neighbouring particles or wall; $\boldsymbol{M}_{c,i}$ is the contact torque, arising from the tangential and normal contact force; $\boldsymbol{R}_i$ is the rotation matrix from the global to the local coordinate system in which the calculation of the rotation expressed by Eq.(2) is accomplished.

As introduced by Favier et al. [27], the non-spherical particles are described by the overlapping multi-sphere model, as shown in Fig. 3. In this way, the interactions between any two non-spherical particles can be simplified as that of spherical particles. In this work the elastic contact force is described by Hertz-Mindlin contact model [34], and the adhesive interaction is accounted for by the JKR theory [31]:

$$F_{JKR} = 4\sqrt{\pi\gamma E^*}a^{3/2} \tag{3}$$

where γ is the surface energy; E^* is the equivalent Young's modulus; a is the contact radius.

3.2. Simulation conditions

The particle system comprises a spreading blade and a base, as shown in Fig. 7. The dimensions of the simulation domain in the spreading and lateral directions are 400D and 10D, respectively. The front and rear boundaries (i.e. $y = 0$ and $y = 10D$ planes) are treated as periodic boundaries for particle flow. The base with length of 400D is made up of clumped cylinders with axes along the y direction, i.e. perpendicular to the spreading direction, where both the distance between adjacent cylinder centres and the cylinder diameter are equal to D. This arrangement is made to provide a fully-rough wall so that sliding of the particles in bulk on the base is mitigated.

The initial particle bed is firstly prepared by using the poured packing method, where approximately 16,000 particles are generated with the size distribution shown in Fig. 2 and the shape shown in Fig. 3. At the start of simulation the blade is lifted vertically to the specified position, forming a vertical gap δ between the spreading blade and layering base, and then moved along x direction with a constant velocity U, by which the particles are spread. The spreading process continues until a particle layer with a length of 300D is obtained.

Considering the size and stiffness (based on Young's modulus of 211 GPa) of the stainless particles, the simulation time step would be too short, requiring unrealistically long simulation time. We therefore follow the criterion proposed by Behjani et al. [36], Hærvig et al. [37] and Washino et al. [38] for scaling down Young's modulus and adhesive surface energy, so that the time step can be increased significantly:

$$\gamma = \gamma_{\exp}\left(\frac{E}{E_{exp}}\right)^{2/5} \tag{4}$$

where $\gamma_{\exp}$ and $E_{\exp}$ are the experimental values and γ and E are the values used in the simulation. So in this work Young's modulus of particles is reduced from 211 GPa to 2.1 GPa, and correspondingly the surface energy γ in the simulation is scaled from 9 mJ/m^2 to 1.4 mJ/m^2 based on Eq.(4). In this way, the simulation time step is increased from 10^{-9} to 10^{-8} s, yielding a computational time of about one week for each case. Other physical properties of particles in the simulation are the same as the measured values and are given in Table1. To evaluate the effect of spreading conditions on the spreading process, the gap δ is varied from 1.5D to 3.0D, and the blade velocity U is set to 0.08 m/s. In order to reduce the effect of blade initial motion, only the last 9 mm (i.e. 200D) length of the particle layer and its spreading process are used for analysis.

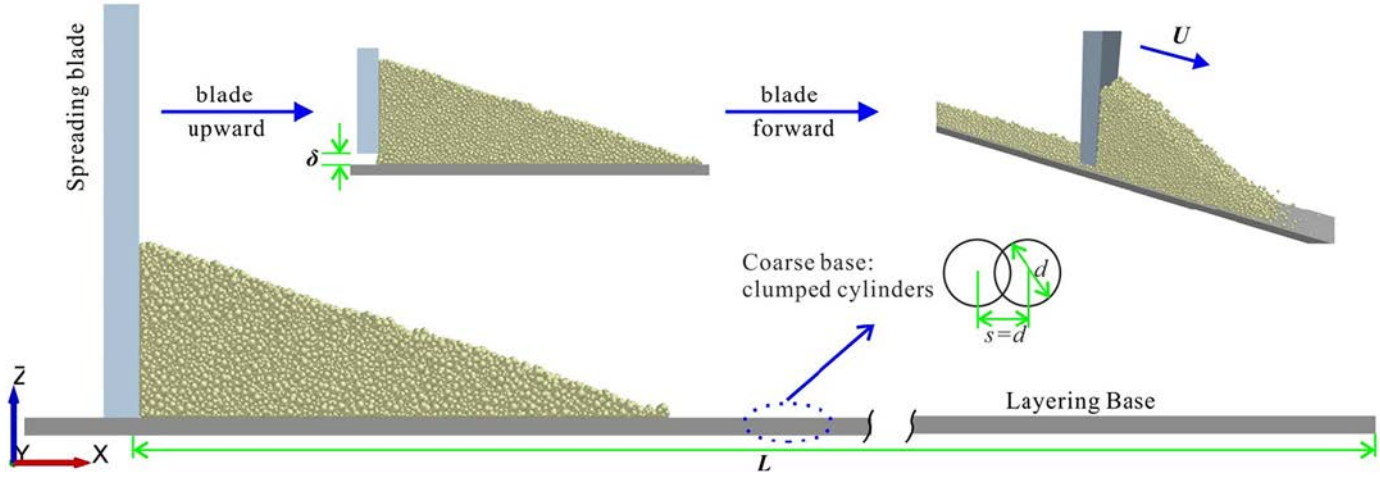

Fig. 7. Schematic of particle spreading process for simulation.

Table1
Particle properties in the simulation.

Parameters	Value
Particle diameter, D (mm)	0.045
Particle density, ρ (kg/m^3)	7980
Young's modulus, E (GPa)	2.1
Poisson ratio, ν	0.3
Friction coefficient, μ	0.5
Restitution coefficient, e	0.64
Surface energy, γ (mJ/m^2)	1.4

4. Simulation results

4.1. Particle dynamics around the blade

As the particle bed is subjected to the horizontal motion of the blade, the dynamics of the particles around the blade tip is analysed. Here, two regions are selected: "before blade" and "under blade", as shown in Fig. 8, where the corresponding particles are in orange colour for illustration. Both regions have the same dimension as the simulation system in y direction, i.e. 10D. The region "before blade" has a length of 6D and height of 6D, while the region "under blade" has a length of 40D and height of δ. To investigate the distribution of the particle velocity, the two regions are divided into bins along the z direction for "before blade" and along the x direction for "under blade". The particle velocity in each bin is averaged for the last 9 mm spreading process to reduce the effect of blade initial motion. As the blade moves in the x direction, only the component of particle velocity in this direction u_x is considered, and it is normalised by the blade speed U.

The region "before blade" is divided into 11 bins in the z direction with height equal to D, and the adjacent bins overlaps 50% in z direction. The variation of particle velocity u_x with height H is shown in Fig. 9. The particle velocity u_x increases with height H and reaches a plateau when the height is larger than $H_1 = \delta + D$. It suggests that the shear band takes up the whole region of $H \le H_1$. At the position of blade tip ($H = \delta$), particle velocity is insensitive to the gap height and is around 0.86 U. At the position closest to the base analysed here ($H/D = 0.5$), the particles are less affected by blade shearing for large gap heights, resulting in a significant decrease of u_x with the increase of the gap height. For the case of $\delta/D = 3.0$, the particle velocity u_x approaches 10% of blade velocity at $H/D = 0.5$, indicating that it could be the lower boundary of the shear band, as suggested by Hare and Ghadiri [39]. This is because it gives a shear band width of around 4D, which is about 5.5 times of the mean volume-equivalent sphere diameter (33.4 μm) of particles used in this work (i.e. based on the total volume of all particles and their

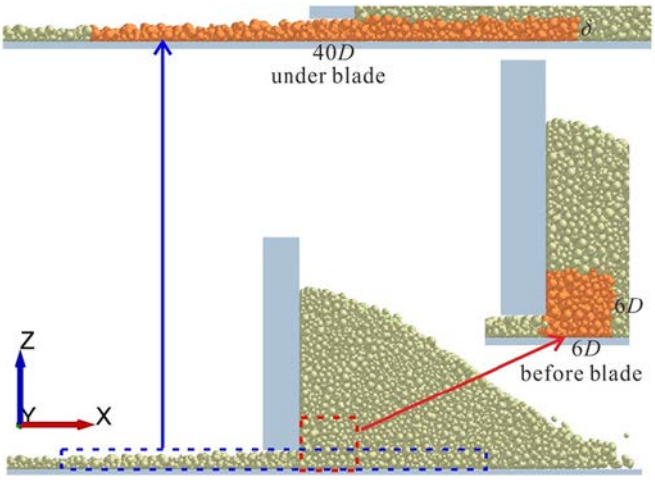

Fig. 8. The illustration of the selected regions around blade: "before blade" and "under blade".

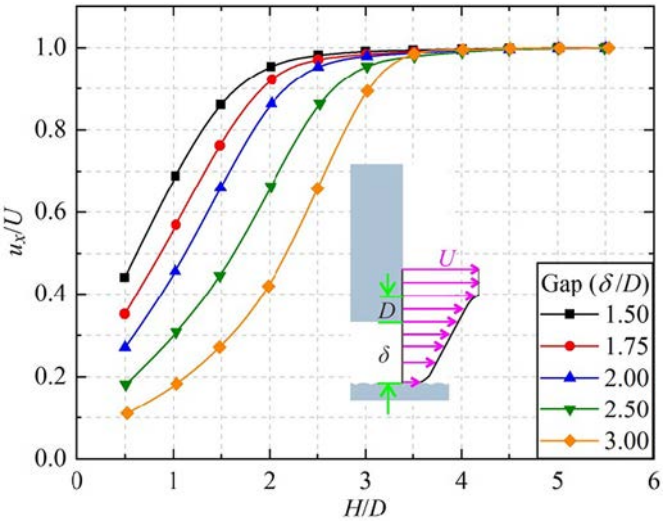

Fig. 9. The variation of u_x with H in the region "before blade" for different gaps.

number). In this way, the velocity profile could be simplified to the schematic diagram shown in Fig. 9. It should be noted that when the gap height is <2.5D, the velocity gradient is about 0.4 U/D and not affected by the gap height. In this case the gap height is much less than the width of shear band of a naturally occurring of fully developed particle flow.

The region "under blade" is divided into 20 bins, side by side in the x direction with bin length of 2D. The variation of particle velocity u_x with the bin position l in the spreading direction is shown in Fig. 10, where l is calculated from the front tip of blade. The particles underneath the blade (i.e. $l < 0$) have positive velocity, indicating they are "dragged" forward by the blade. This dragging mechanism has also been reported by Haeri et al. [22], who used it to guide the optimisation of blade geometry [25]. For $l/D < -3$ there is not much difference in particle velocity for different gap heights except for the largest one, where the dragging effect is smallest. The particle velocity increases exponentially to the maximum at $l/D = 2$, and then decreases gradually to a plateau for all gap heights, except the largest one, which continues to rise, albeit at a much slower rate. There is a very sharp rise in particle velocity u_x in the bins across the front tip of blade (i.e. l/D from −1 to 1). Although the blade motion has more influence at $l/D = 1$ than other positions, nevertheless the velocity gradient here (i.e. 0.1 U/D) is much smaller

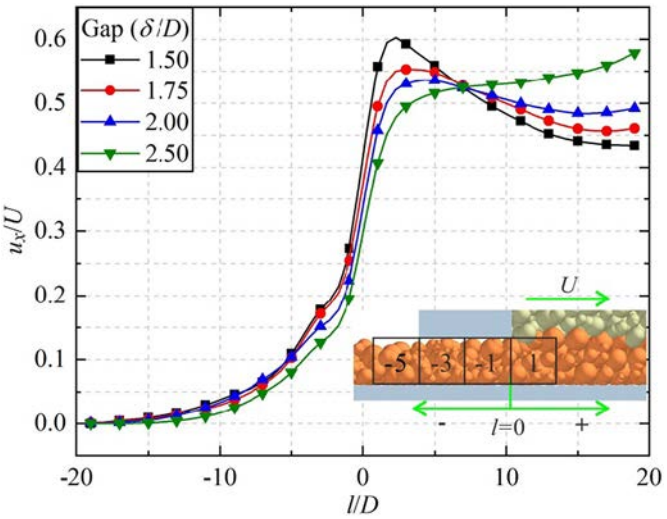

Fig. 10. The variation of u_x with l in the region "under blade" for different gaps.

than the one in the z direction for the region "before blade" shown in Fig. 9 (i.e. 0.4 U/D).

4.2. Empty patches in the particle spread layer

Fig. 11 shows the locally zoomed part of the particle layer deposited by the blade, where the particles are coloured based on their volume. A number of empty patches with different sizes could be found along the spreading direction, especially for the case of $\delta/D = 1.5$. With the increase of gap height, the particle layer becomes more uniform with fewer patches and large particles are more prevalent. Empty patches are clear manifestation of jamming in the regions around the blade. It is worth pointing out that as a consequence of jamming in the case of narrow gaps the heap before the blade is enriched with large particles, a situation akin to segregation. Absence of large particles in the case of $\delta/D = 1.5$ is indicative of large particles being accountable for jamming. To consider the effect of presence of large particles in the particle size distribution, the total particle volume V_{pt} spread over the work surface is considered here instead of particle number, as shown in Fig. 12. The fractional coverage increases linearly with the gap height and correlates well with the linear equation shown in Fig. 12. This implies that the total solid fraction remains constant. However, it should be noted that this is an average value and does not represent the spatial distribution of the spread particles over the work surface. This linear relationship is also found for the dependence of the mean mass flow rate with gap height, which is not shown here for brevity. The fitting equation in Fig. 12 suggests that the total particle volume/number approaches zero at $\delta_C = 1.0D$, which is about 1.35 times of equivalent-volume sphere diameter of particles (i.e. 33.4 μm).

To detect the location of the empty patches, the spread particle layer is divided into a number of bins in the x and y directions with $\Delta x = 2D$ and $\Delta y = 1.25D$, with adjacent bins overlapping by 50% in both directions. In this way, only the empty patches larger than 2D in the spreading direction are considered. Based on the particle volume, an individual bin is assumed as an empty patch if its particle fraction is very low and meets the following criterion:

$$\frac{\sum Vp}{\Delta x \times \Delta y \times (\delta - \delta_c)} < 0.1 \tag{5}$$

where $\delta_C = 1.0D$ is the critical gap. The distribution of empty patches along the spreading direction x is shown in Fig. 13, where every legend underneath each δ/D figure indicates that there is at least one empty patch in its y direction. The location x of the legends correlates well

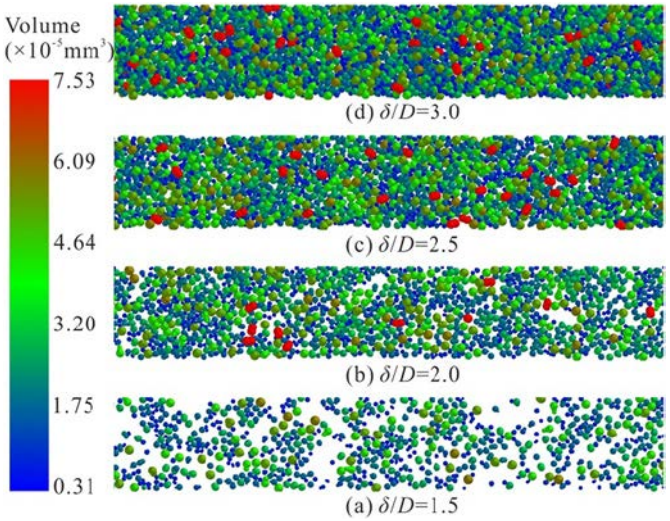

Fig. 11. The images of locally zoomed part of the particle layer.

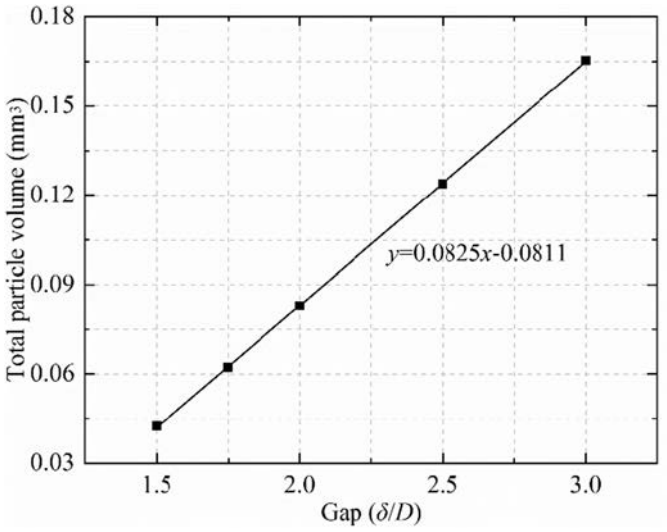

Fig. 12. The variation of the total particle volume deposited by the blade with gap height.

with the presence of the empty patches visible in the corresponding images. It suggests that the criterion given by Eq.(5) is reasonable to predict the location x of empty patches. The legends are not continuously connected along the spreading direction. Some are connected to each other in some location, and others are isolated at other places. The location x with no legend indicates that there is no empty patch here. Fig. 13 also shows that the total number of empty patches decreases sharply with increasing gap height. There are no empty patches for the case with $\delta/D = 3.0$, and therefore this case is not included here.

The connected legends, i.e. with no break between them, in Fig. 13 are likely to belong to the same empty patch. Assuming this to be the case, their number and length could be calculated. As the adjacent bins overlap by 50% and the size of an individual bin is $\Delta x = 2D$, i number of legends correspond to an empty patch with length of $(i + 1)D$. For example, the longest empty patch for $\delta/D = 1.5$ is located at about $x/D = 190$ with 12 connected legends, indicating that this empty patch has 12 overlapping bins with total length of 13D. Based on the number of the empty patches N_{ep} and the total spreading time t, the variation of the frequency of the empty patches (i.e. N_{ep}/t) with their length is shown in Fig. 14. The frequency of empty patches decreases sharply with their length. With the increase of gap height, the maximum length of the patch decreases sharply. For example, the longest patch is only 4-5D for the case with $\delta/D = 2.0$, whilst for the case with $\delta/D = 1.5$, it is actually the mean length that is about 4-5D. The frequency of small patches also decreases sharply with the increase of gap height. These results show that both the probability of the formation of patches and their mean length increase sharply with the decrease of the gap height. Fig. 14 also shows that with the increase of gap height, the empty patches are mainly composed of smaller empty patches. This could also be observed from Fig. 15, where the probability of the number of empty patches for each patch length is given. Longer patches occur less frequently and vice versa. Considering that the empty patches are manifestation of jamming before the blade, as intuitively expected, both the jamming frequency and duration of each jamming decrease as the gap height is increased. Further work is needed to elucidate the role of particle shape and cohesion in affecting this temporal behaviour.

4.3. Formation mechanics of empty patches

The occurrence of empty patches of the spread particle layer could be related to the transient jamming of particles. During the survival period of jamming the particle flow through the gap is transiently halted locally, and a strong contact force network is developed. Observations of simulation videos show that as the blade continues its forward movement,

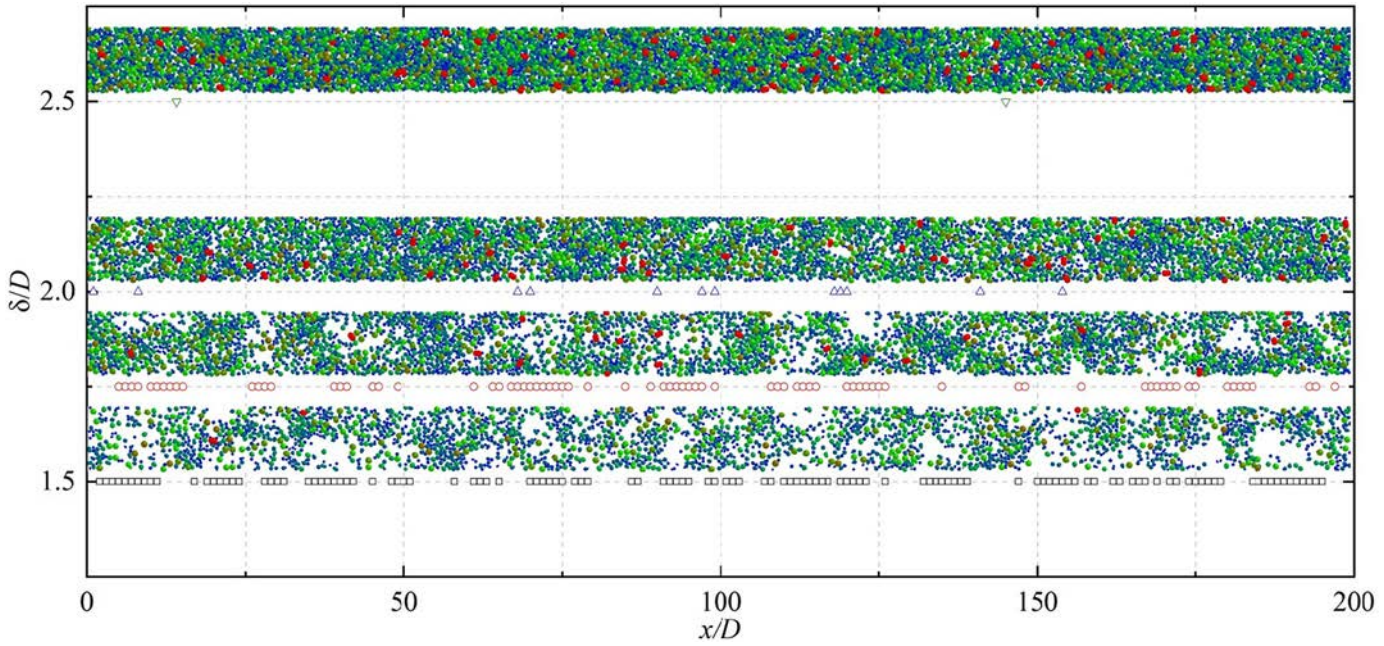

Fig. 13. Empty patches along the particle spreading direction.

such arches collapse and some particles 'fly' through the gap in the opposite direction of the blade motion. In this way, they eventually collide with and displace stationary particles, disturbing the spread layer.

Transient jamming of particles before the blade is analysed by monitoring the mass flow rate through the gap. There are a number of time periods within which the mass flow rate is zero, indicating that particle jamming may have occurred in this period. By examining the duration of this period, the number of jamming events N_j with survival time of Δt_j could be estimated. Based on the total spreading time t, the variation of the frequency of the jamming events (i.e. N_j/t) with their duration is shown in Fig. 16, where Δt_j is normalised by the characteristic time scale $t_0 = D/U$ (i.e. 5.625×10^{-4} s). For the case with $\delta/D = 1.5$, the frequency decreases exponentially with Δt_j. It suggests that jamming events with shorter durations occur at higher frequencies while the ones with longer durations occur at lower frequencies. The maximum value of Δt_j for $\delta/D = 1.5$ is about $0.56t_0$ with frequency of about 9 Hz. With the increase of gap height, both the maximum duration of jamming and the frequency of small survival times of jamming decrease. For the case with $\delta/D = 3.0$, although there are no empty patches with a length larger than $2D$ as discussed above, the frequency of small survival times of jamming is nevertheless non-zero. The jamming with survival time larger than $0.2t_0$ may be much more effective for the formation of empty patches of the spread particle layer than that of the smaller survival time of jamming with a larger frequency.

Although the transient survival time of jamming is short (i.e. in the order of 10^{-4} s), it could result in particles with a large velocity in the opposite direction of blade motion, a situation akin to bursting. To examine this effect, the momentum of particles in the x direction in the wake of the blade is shown in Fig. 17, where the momentum p_x is normalised by an individual particle with diameter of D and velocity of U:

$$p_x = \frac{\sum m u_x}{m_0 U} \tag{6}$$

where m is the mass of an individual particle and m_0 is the mass of an particle with diameter of D. For the case with $\delta/D = 1.5$, there are a number of large peaks with negative momentum, where the particles have large negative velocity u_x. This is a consequence of the collapse of

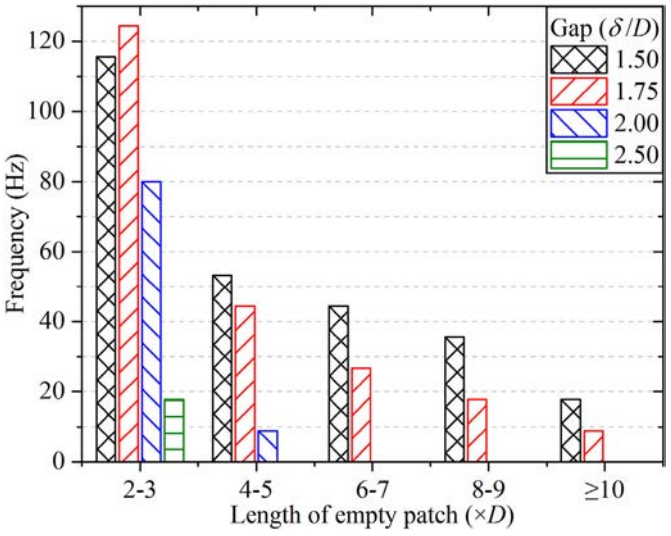

Fig. 14. Frequency of empty patches with each patch length.

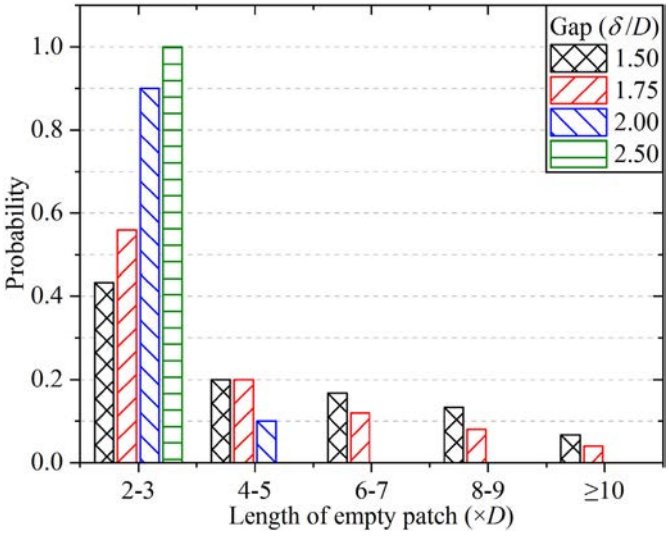

Fig. 15. Probability distribution of the number of empty patches with each patch length.

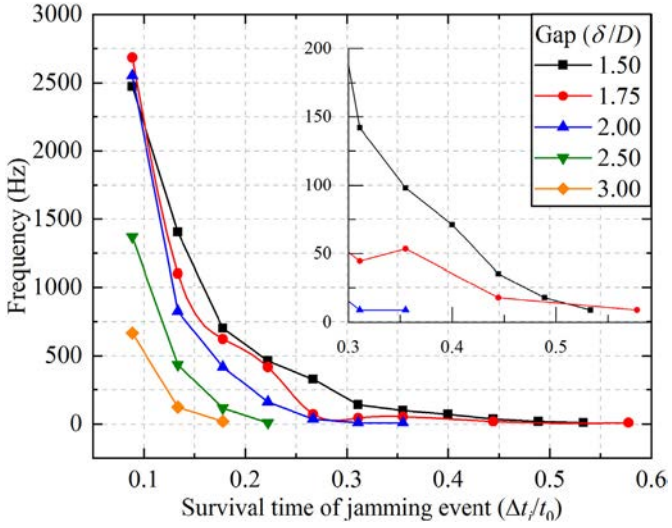

Fig. 16. Frequency distribution of jamming with each survival time.

arches, following jamming, and in some instances, they give rise to 'flying' particles, which collide with other particles, as shown in the zoomed images of the top view of the spread layer in Fig. 17. Therefore, jamming-induced bursts could contribute to the formation of empty patches too. For example, a jamming with a survival time of $0.2t_0$ would be expected to lead to an empty patch with $0.2D$ if it merely stopped the particle flow; so empty patches larger than $2D$ are indicative of particle bursts. With the increase of gap height, the number of negative peaks decreases sharply. However an arch collapse does not necessarily give rise to bursts of particles.

5. Conclusions

The particle spreading process in the additive manufacturing has been analysed using DEM simulations. The particles physical and mechanical properties have been characterised for use the simulations, and Young's modulus and surface energy have been scaled down to speed up the simulations. The spreading gap has been varied and its effect on spreading has been analysed and quantified in terms of particle velocity around blade and empty patches formed in the spread particle layer. The main results from the present study are summarised as follows:

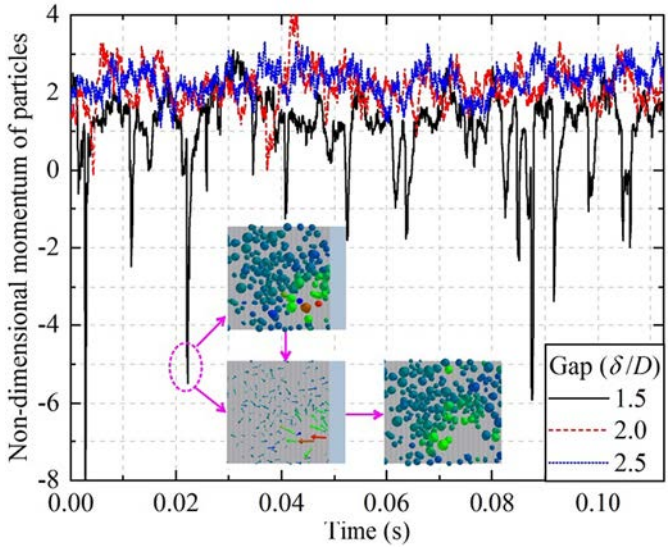

Fig. 17. The variation of the momentum of particles in x direction with time.

1) For the particles before the blade, the particle velocity near the base decreases with the increase of gap height, and the width of the shear band for a fully developed particle flow is about $4D_{90}$. The particles underneath the blade are "dragged" forward by blade, and the particle velocity has a jump across the front tip of blade.
2) The total particle volume of the spread particle layer increases linearly with the gap height. Large empty patches on the spread particle layer are found along the spreading direction for small gap heights. Narrow gaps have a segregation influence on the heap before the blade. The frequency of empty patches decreases exponentially with their length and both the probability of the formation of patches and their mean length increase sharply with the decrease of the gap height.
3) The empty patches of the spread particle layer are caused by particle jamming in the region before blade. Its collapse leads in some instances to particle bursts after the blade. The frequency of jamming decreases exponentially with its survival time, and total jamming probability decreases sharply with the gap height. The jamming with a large duration may be much more effective for the formation of empty patches than that of the smaller survival time of jamming with a larger frequency.

Acknowledgments

We are grateful to Dr Martin Kearns, Powders Group Director of Sandvik Osprey Ltd, for providing a sample of gas-atomised stainless steel particles for characterisation of their physical and mechanical properties to be used in the simulations. We are also thankful to DEM Solutions, Edinburgh, UK, for providing a special license for the EDEM software for use in this work. The support of the EPSRC Programme Grant: Friction: The Tribology Enigma (EP/R001766/1) and the Virtual Formulation Laboratory Grant of the EPSRC Future Formulation Programme (EP/N025261/1) is gratefully acknowledged.

The publication of this article coincided with the sad news of the untimely passing away of Professor Robert Behringer, Duke University, USA. This article is dedicated to his memory. His pioneering work on jamming in granular materials inspired this work.

References

[1] W.E. Frazier, Metal additive manufacturing: a review, J. Mater. Eng. Perform. 23 (2014) 1917–1928.
[2] W. Gao, Y. Zhang, D. Ramanujan, K. Ramani, Y. Chen, C.B. Williams, C.C.L. Wang, Y.C. Shin, S. Zhang, P.D. Zavattieri, The status, challenges, and future of additive manufacturing in engineering, Comput. Aided Des. 69 (2015) 65–89.
[3] D.D. Gu, W. Meiners, K. Wissenbach, R. Poprawe, Laser additive manufacturing of metallic components: materials, processes and mechanisms, Int. Mater. Rev. 57 (2013) 133–164.
[4] N. Guo, M.C. Leu, Additive manufacturing: technology, applications and research needs, Front. Mech. Eng. 8 (2013) 215–243.
[5] I. Gibson, D. Rosen, B. Stucker, Additive Manufacturing Technologies, 3D Printing, Rapid Prototyping, and Direct Digital Manufacturing, Springer, 2015.
[6] T.D. Ngo, A. Kashani, G. Imbalzano, K.T.Q. Nguyen, D. Hui, Additive manufacturing (3D printing): a review of materials, methods, applications and challenges, Compos. Part B 143 (2018) 172–196.
[7] S. Singh, S. Ramakrishna, R. Singh, Material issues in additive manufacturing: a review, J. Manuf. Process. 25 (2017) 185–200.
[8] T. Debroy, H.L. Wei, J.S. Zuback, T. Mukherjee, J.W. Elmer, J.O. Milewski, A.M. Beese, A. Wilson-Heid, A. De, W. Zhang, Additive manufacturing of metallic components – process, structure and properties, Prog. Mater. Sci. 92 (2018) 112–224.
[9] J.R. Tumbleston, D. Shirvanyants, N. Ermoshkin, R. Janusziewicz, A.R. Johnson, D. Kelly, K. Chen, R. Pinschmidt, J.P. Rolland, A. Ermoshkin, E.T. Samulski, J.M. Desimone, manufacturing. Additive, Continuous liquid interface production of 3D objects, Science 347 (2015) 1349–1352.
[10] K.V. Wong, A. Hernandez, A review of additive manufacturing, ISRN Mechanical Engineering 2012 (2012) 1–10.
[11] I. Yadroitsev, A. Gusarov, I. Yadroitsava, I. Smurov, Single track formation in selective laser melting of metal powders, J. Mater. Process. Technol. 210 (2010) 1624–1631.
[12] S.M. Thompson, L. Bian, N. Shamsaei, A. Yadollahi, An overview of direct laser deposition for additive manufacturing; part I: transport phenomena, modeling and diagnostics, Additive Manufacturing 8 (2015) 36–62.
[13] G. Enstad, On the theory of arching in mass flow hoppers, Chem. Eng. Sci. 30 (1975) 1273–1283.
[14] R.P. Behringer, Jamming in granular materials, Comptes Rendus Physique 16 (2015) 10–25.

[15] Y.S. Lee, P. Nandwana, W. Zhang, Dynamic simulation of powder packing structure for powder bed additive manufacturing, Int. J. Adv. Manuf. Technol. 96 (2018) 1507–1520.
[16] W.H. Lee, Y. Zhang, J. Zhang, Discrete element modeling of powder flow and laser heating in direct metal laser sintering process, Powder Technol. 315 (2017) 300–308.
[17] C. Qiu, C. Panwisawas, M. Ward, H.C. Basoalto, J.W. Brooks, M.M. Attallah, On the role of melt flow into the surface structure and porosity development during selective laser melting, Acta Mater. 96 (2015) 72–79.
[18] M.M. Francois, A. Sun, W.E. King, N. Henson, D. Tourret, C.A. Bronkhorst, N.N. Carlson, C.K. Newman, T. Haut, J. Bakosi, J.W. Gibbs, V. Livescu, S.A. Vander Wiel, A. Clarke, M.W. Schraad, T. Blacker, H. Lim, T. Rodgers, S. Owen, F. Abdeljawad, J. Madison, A.T. Anderson, J.L. Fattebert, R.M. Ferencz, N.E. Hodge, S.A. Khairallah, O. Walton, Modeling of additive manufacturing processes for metals: challenges and opportunities, Curr Opin Solid St M 21 (2017) 198–206.
[19] H.W. Mindt, O. Desmaison, M. Megahed, A. Peralta, J. Neumann, Modeling of powder bed manufacturing defects, J. Mater. Eng. Perform. 27 (2017) 32–43.
[20] A. Townsend, N. Senin, L. Blunt, R.K. Leach, J.S. Taylor, Surface texture metrology for metal additive manufacturing: a review, Precis. Eng. 46 (2016) 34–47.
[21] S.A. Khairallah, A.T. Anderson, A. Rubenchik, W.E. King, Laser powder-bed fusion additive manufacturing: physics of complex melt flow and formation mechanisms of pores, spatter, and denudation zones, Acta Mater. 108 (2016) 36–45.
[22] S. Haeri, Y. Wang, O. Ghita, J. Sun, Discrete element simulation and experimental study of powder spreading process in additive manufacturing, Powder Technol. 306 (2016) 45–54.
[23] E.J.R. Parteli, T. Pöschel, Particle-based simulation of powder application in additive manufacturing, Powder Technol. 288 (2016) 96–102.
[24] Z. Xiang, M. Yin, Z. Deng, X. Mei, G. Yin, Simulation of forming process of powder bed for additive manufacturing, J. Manuf. Sci. Eng. 138 (2016), 081002. .
[25] S. Haeri, Optimisation of blade type spreaders for powder bed preparation in additive manufacturing using DEM simulations, Powder Technol. 321 (2017) 94–104.
[26] H. Chen, Q. Wei, S. Wen, Z. Li, Y. Shi, Flow behavior of powder particles in layering process of selective laser melting: numerical modeling and experimental verification based on discrete element method, Int. J. Mach. Tools Manuf. 123 (2017) 146–159.
[27] J.F. Favier, M.H. Abbaspour-Fard, M. Kremmer, A.O. Raji, Shape representation of axi-symmetrical, non-spherical particles in discrete element simulation using multi-element model particles, Eng. Comput. 16 (1999) 467–480.
[28] M. Pasha, C. Hare, M. Ghadiri, A. Gunadi, P.M. Piccione, Effect of particle shape on flow in discrete element method simulation of a rotary batch seed coater, Powder Technol. 296 (2016) 29–36.
[29] M. Ghadiri, Hardness, Stiffness, and roughness of Particles, in: M. Hiroaki, K. Higashitani, H. Yoshida (Eds.), Powder Technology Handbook, Third EditionCRC Press, New York, 2006.
[30] U. Zafar, C. Hare, A. Hassanpour, M. Ghadiri, Drop test: a new method to measure the particle adhesion force, Powder Technol. 264 (2014) 236–241.
[31] K. Johnson, K. Kendall, A. Roberts, Surface energy and the contact of elastic solids, Proceedings of the Royal Society of London. A. Mathematical and Physical Sciences, 324, 1971, pp. 301–313.
[32] I.F. Sbalzarini, P. Koumoutsakos, Feature point tracking and trajectory analysis for video imaging in cell biology, J. Struct. Biol. 151 (2005) 182–195.
[33] P.A. Cundall, O.D.L. Strack, A discrete numerical model for granular assemblies, Géotechnique 29 (1979) 47–65.
[34] C. Thornton, Granular Dynamics, Contact Mechanics and Particle System Simulations, Springer, New York, 2015.
[35] W. Nan, M. Ghadiri, Y. Wang, Analysis of powder rheometry of FT4: effect of air flow, Chem. Eng. Sci. 162 (2017) 141–151.
[36] M.A. Behjani, N. Rahmanian, N. Fardina Bt Abdul Ghani, A. Hassanpour, An investigation on process of seeded granulation in a continuous drum granulator using DEM, Adv. Powder Technol. 28 (2017) 2456–2464.
[37] J. Hærvig, U. Kleinhans, C. Wieland, H. Spliethoff, A.L. Jensen, K. Sørensen, T.J. Condra, On the adhesive JKR contact and rolling models for reduced particle stiffness discrete element simulations, Powder Technol. 319 (2017) 472–482.
[38] K. Washino, E.L. Chan, T. Tanaka, DEM with attraction forces using reduced particle stiffness, Powder Technol. 325 (2018) 202–208.
[39] C. Hare, M. Ghadiri, Stress and strain rate analysis of the FT4 powder rheometer, EPJ Web of Conferences 140 (2017), 03034. .